Single and double ionization of magnesium via four-photon excitation of the $3p^2\ ^1S_0$ autoionizing state: Experimental and theoretical analysis

I. Liontos, A. Bolovinos,* S. Cohen, and A. Lyras
Atomic and Molecular Physics Laboratory, Physics Department, University of Ioannina, 45110 Ioannina, Greece
(Received 30 April 2004; published 10 September 2004)

Single and double ionization of ground state Mg atoms is observed in an atomic beam experiment in the 584–596 nm spectral range with a maximum intensity of 9×10^{11} W/cm^2 and pulses of ns duration. The Mg^+ spectrum consists of a single broad resonance whose position is very sensitive to laser intensity and it is attributed to the four-photon excitation of the doubly excited $3p^2\ ^1S_0$ state. For intensities higher than 2×10^{11} W/cm^2 a considerable double ionization yield is obtained. The Mg^{2+} spectra are composed of two lobes, each one dominating at different intensities. These observations can be interpreted by a sequential mechanism in which doubly charged ions are created by multiphoton resonant ionization of the excited $3p_{1/2,3/2}$ Mg^+ states (with negligible contribution from the $3s_{1/2}$ ionic ground state) after the single ion production has saturated. The population of these excited ionic states suggests the absorption of two photons above the first ionization threshold of Mg. This interpretation is unambiguously confirmed by a complementary fluorescence experiment. Moreover, both ionization and fluorescence spectra as well as ionization yields are very well reproduced by a theoretical model based on a combination of density matrix and rate equations, taking into account the near-resonant coupling between the $3p^2\ ^1S_0$ and $3p3d\ ^1P_1$ autoionizing states and employing calculated parameters for both Mg and Mg^+. It is thus pointed out that for visible ns pulses of moderate intensity the autoionizing resonances play a crucial role in the multiphoton sequential double ionization of alkaline-earth-metal atoms.

DOI: 10.1103/PhysRevA.70.033403 PACS number(s): 32.80.Rm, 32.80.Dz, 33.80.Rv

I. INTRODUCTION

Multiphoton single and double ionization of alkaline-earth-metal atoms is a subject of continuing experimental and theoretical investigations. The interest originates from the earliest experimental observations [1] where it was demonstrated that the yield of doubly charged ions was surprisingly large compared to the singly charged ion yield at moderate laser intensities ($<10^{13}$ W/cm^2). Multiple multiphoton ionization of rare gases has been also intensively investigated [2] using ultrashort pulses and very high intensities ($>10^{13}$ W/cm^2), due to the fact that their high ionization potentials prevent ionization at low intensities. Moreover, at such high intensities the details of the atomic structure of the rare gases do not seem to play a crucial role in the multiple ionization process. On the other hand, multiphoton double ionization of alkaline earth atoms (for a recent review see Ref. [3]) presents an interesting alternative to those studies and the reason for this is twofold. First, because of their low first and second ionization thresholds a relatively small number of photons are required for their double ionization and second, their energy spectrum just above the first ionization threshold contains dense manifolds of doubly excited states. Due to the fact that those states exhibit a high degree of electron correlation they are expected to contribute to the formation of doubly charged ions. In particular, resonant excitation of these autoionizing states could lead to the absorption of a number of additional photons above the first ionization threshold, in excess of the minimum number required to ionize ground state atoms. It was anticipated that this additional photon absorption could possibly lead to the simultaneous removal of the two valence electrons; a process usually termed direct double ionization. However, apart from very few exceptions [4], all experiments in alkaline earth atoms, performed with visible ns or ps laser pulses and having detected ions, electrons or fluorescence, revealed that no more than one photon for Ca, Sr, and Ba [3] and up to two photons for Mg [5–8] are absorbed above the first ionization threshold leading to the population of ground as well as excited ionic states. Doubly charged ions are then produced by the multiphoton ionization of those ionic states, i.e., sequentially. Nevertheless, there is a series of published experimental studies (in Ba and Sr), performed with ~40 ns infrared pulses, where the authors claim they have observed direct double ionization [9].

Among the alkaline-earth-metal atoms, Mg combines experimental convenience and accurate theoretical description. First, the single and double ionization thresholds are still within experimental reach with moderate intensity lasers. Second, due to the absence of a d_j ionic state the doubly excited levels structure just above the first ionization potential is much simpler compared to that of the heavier Ca, Sr, and Ba atoms. There are a number of earlier studies dealing with double multiphoton ionization of Mg, performed with ns [5,6], ps [7,8] or fs [10,11] pulses. In Ref. [10] it was pointed out that even with such short pulses (150 fs at 400 nm) two-electron effects may still be important in order to interpret the experimental findings. Double ionization of Mg via four-photon excitation of the $3p^2\ ^1S_0$ autoionizing state was experimentally investigated previously with 30 ps pulses and photoelectron detection [7]. It was claimed that

*Electronic address: abolovin@cc.uoi.gr

 ©2004 The American Physical Society

five- or six-photon absorption in the continuum was evidenced, indicating the possibility of direct double ionization. Motivated by this observation, van Druten *et al.* [8] repeated the experiment under similar conditions and 1 ps laser pulses but the aforementioned five-photon absorption was not verified. They found however, clear evidence of two-photon absorption above the first ionization threshold, leading to the formation of Mg^+ in the first excited $3p_{1/2,3/2}$ ionic states. It was recognized that the $3p^2\ ^1S_0$ state played an important role in the two-photon above-threshold absorption but this role was not investigated in detail. Moreover, the theoretical interpretation was qualitative and the observed photoelectron energy shifts were compared with theoretical estimates taking into account only the ponderomotive potentials.

The present paper aims at investigating in detail the same spectral range but with relatively long (ns) pulsed excitation and laser intensities that are an order of magnitude lower ($10^{11}-10^{12}$ W/cm^2) than those employed in earlier experiments with shorter (ps) pulses. Under our presumed unfavorable conditions, a considerable amount of double ionization has been recorded. It turns out that, for intensities above a certain threshold value, the near-resonant radiative coupling between the doubly excited $3p^2\ ^1S_0$ and $3p3d\ ^1P_1$ states, that unfolds over a relatively long time interval, plays a dominant role in the dynamics of the atom-field interaction, despite the presence of a competing fast decaying autoionization process, and contributes significantly to the production of excited ionic states. From then on, the production of doubly charged ions depends critically on resonantly enhanced multiphoton excitation within the Mg ion. We obtain supporting evidence from an independent fluorescence experiment and gratifying agreement with the results of a sufficiently detailed theoretical model based on a combination of atomic density matrix and ionic rate equations, taking into account all the autoionization and radiative couplings among judiciously chosen atomic and ionic states. Therefore, we have explicitly, unambiguously and quantitatively shown that the rich autoionizing structure of Mg contributes to significant sequential double ion production, under specific excitation conditions not thoroughly examined in the past.

The rest of paper is divided in four sections: In the following section, the experimental setup and procedures are briefly presented. In the third section we describe the theoretical model for the laser-atom-ion dynamics as well as the methods used for the evaluation of the atomic and ionic parameters employed in the dynamical equations. In the fourth section, our experimental results for the Mg^+, Mg^{2+}, and fluorescence yields, as a function of both laser frequency and intensity, are presented and compared with theoretical predictions. Finally, in the last section our conclusions are given.

II. EXPERIMENTAL SETUP AND PROCEDURE

The experimental setup is shown schematically in Fig. 1(a). It includes an atomic beam apparatus where the Mg single and double photoionization experiments have been performed and a Mg vapor cell devoted to the studies of fluorescence detection. In both experiments the laser radiation is provided by a Nd:YAG pumped dye laser (Lambda Physik Scanmate 2EC-400 pumped by Brilliant BW) operating in the 584–596 nm wavelength range (Exciton's Rhodamin 610 dye) and offering wavelength calibration within $\sim$0.01 Å. The laser linewidth is $\sim$0.1 cm^{-1} and the amount of amplified spontaneous emission (ASE) is kept to a power level lower than 1.5% by appropriately adjusting the dye concentration of the laser oscillator and amplifier. The system operates at a repetition rate of 10 Hz and it delivers linearly polarized pulses of $\sim$5 ns duration. The pulse energy is measured by a digital joule-meter (Opphir Model PD300) and its maximum value is $\sim$30 mJ. The latter corresponds to a maximum power density of $\sim 4\times10^{11}$ or $\sim 9\times10^{11}$ W/cm^2 when the laser beam is focused in the interaction region by an $f=15$ cm or $f=10$ cm focal length lens, respectively. The power density is estimated under the assumption of a diffraction limited Gaussian beam profile. The laser beam energy is controlled by a variable attenuator (Newport Model 735-5) without any spatial misalignment.

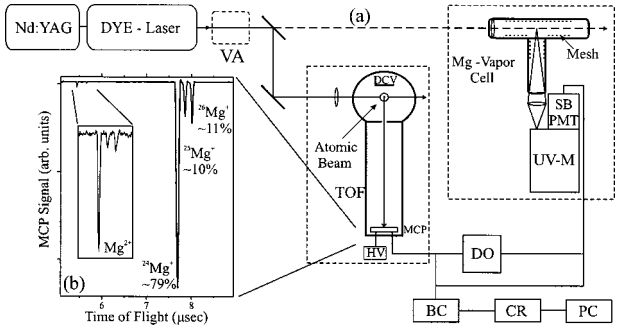

FIG. 1. (a) Schematic diagram of the experimental setup. TOF, time-of-flight mass spectrometer; DCV, DC ion repeller voltage; MCP, microchannel plates; HV, high voltage power supply for MCPs; VA, variable attenuator; UV-M, ultraviolet monochromator; SB PMT, solar blind photomultiplier tube; DO, digital oscilloscope; BC, boxcar integrator; CR, chart recorder; PC, personal computer. (b) Typical TOF mass spectra.

The pumping system for either the atomic beam chamber or the cell consists of a rotary pump and a 120 l/min turbo molecular pump (Leybold Turbovac 151), while the chamber is also equipped with a liquid nitrogen trap. The achieved background pressure is $\sim10^{-6}$ mbar. In the atomic beam experiment Mg (Aldrich 99.98%) vapor is produced in an electrically heated stainless steel oven at the top of the chamber and connected to it through a water-cooled baffle. The oven operates below the Mg melting point and its temperature (580–600 °C) is continuously monitored by a thermocouple. The vapor passes through a 0.5 mm diameter hole where it is collimated via a stainless steel tube (length 10 cm, diameter 5 mm). About 3 cm downstream from the tube exit the atomic and laser beams intersect perpendicularly. The atomic density at that point (as estimated by geometrical considerations) is $\sim10^8$ atoms/cm^3. The ions created by the laser-atom interaction are detected in a direction perpendicular to both the atomic and laser beams and they are discriminated according to their mass-to-charge ratio using a time-of-flight (TOF) mass spectrometer. The TOF setup consists of a repeller electrode biased at a positive DC voltage, creating a field

strength ~70 Volts/cm which pushes the ions towards a grounded plate with a 2 mm diameter hole in its center. Following the plate is a 20 cm long grounded tube at the end of which a dual microchannel plate detector (MCP) is mounted. The TOF system is capable of resolving all three singly and doubly ionized Mg isotopes $^{24,25,26}Mg^{+}$ and $^{24,25,26}Mg^{2+}$ [see Fig. 1(b)]. The MCP detector output signal is monitored by a digital oscilloscope (LeCroy 9310), processed by a boxcar integrator (Stanford Research Systems SR 250) and fed to a chart recorder (Yokogawa LR4120) and a personal computer where the data are finally stored.

Space charge effects at the low atomic density mentioned above are found to be weak. However, they are not completely eliminated as evidenced by the small broadening of the width of the $^{24}Mg^{+}$ TOF peak with increasing laser pulse energy. On the other hand, further reduction of the atomic density results in very low Mg^{2+} signal levels.

After each new load of the oven with Mg, a small TOF peak of $^{23}Na^{+}$ ions appears which lasts for about 2 days of operation and then it disappears. The problem of $^{23}Na^{+}$ presence was also encountered in previous experiments and prevented a reliable measurement of Mg^{+} spectra and intensity dependence [8]. All the measurements reported here on Mg^{+} were recorded under Na^{+} free conditions. However the TOF mass spectra show additionally a small contamination of H^{+} and $^{12}C^{+}$ ions, probably originating from the hot parts of the chamber or hydrocarbons present in the interaction region. Most important is the presence of the singly charged carbon ions because they have the same mass-to-charge ratio with the strongest $^{24}Mg^{2+}$ isotope and therefore it was necessary to take a number of measures for their contribution to the measured doubly charged Mg signal to be eliminated or at least evaluated. First, the wavelength dependence of $^{12}C^{+}$ was recorded under conditions where neither Mg^{2+} nor Mg^{+} was detected. The spectrum is unstructured consisting of a flat background. Second, the operation of the liquid nitrogen trap eliminatess the H^{+} and $^{12}C^{+}$ signal at low atomic densities and greatly reduces it at the highest density employed here. Third, it was noted that under a variety of conditions with no Mg^{2+} or Mg^{+} present the H^{+}/C^{+} ratio is always ~0.6. Using this fact, the amount of $^{12}C^{+}$ on the $m/Z=12$ TOF peak could be estimated. Its contribution is found to be less than 3%. Nevertheless, the $^{24}Mg^{2+}$ measurements were corrected by this factor. On the other hand, no correction is necessary for the $^{25}Mg^{2+}$ peak for which $m/Z=12.5$ and, moreover, after the aforementioned small correction the three $^{24,25,26}Mg^{2+}$ isotopes (and the $^{24,25,26}Mg^{+}$ ones) exhibit the known natural abundance percentage (79%, 10%, and 11%, respectively).

For the experiments involving detection of fluorescence the dye laser output is focused into a quartz T-shaped tube in which Mg undergoes continuous evaporation. The $f=10$ cm focusing lens is mounted inside the tube. The Mg vapor density is determined by measuring the temperature of the cell via a thermocouple in contact with it at its center. Coating of the quartz windows with Mg is prevented by the use of a metallic mesh rolled around its main body and by the presence of ~3 Torr He buffer gas (slightly higher than the Mg vapor pressure). Under these conditions the recorded data are reproducible for about 2 days. Then the cell had to be cleaned and refilled with Mg pellets. The metal vapor fluorescent light is collected at 90° with respect to the laser beam direction and analyzed by a McPherson 218 monochromator equipped with an EMI solar-blind photomultiplier tube (PMT) (model RFIB214FV). In order to avoid scattered laser light entering the PMT an appropriate UV neutral density filter is placed in front of it. The signal from the photomultiplier is amplified (Ortec 485) and then fed to a boxcar integrator and the averaged output is recorded on a chart recorder and stored into a personal computer.

III. THEORETICAL MODEL

In order to interpret the experimental data we have developed a theoretical model, sufficiently detailed to describe the dynamics of the Mg atom and the Mg^{+} ion when irradiated by the laser pulses. The complete set of dynamic equations, shown below, combines six equations [Eqs. (1)–(6)], resulting from a density matrix model for the Mg atom, with three rate equations for the Mg^{+} time evolution [(7)–(9)]. We will not present a detailed derivation, since it is well documented in the literature, to which we will refer where necessary. Instead, we will briefly explain the meaning of the various terms in the equations and qualitatively explain their contribution to the dynamics, when appropriate, with the help of the detailed excitation scheme depicted in Fig. 2.

$$\dot{\sigma}_{11} = -(\gamma_{1i}^{(4)} + \gamma_{1b}^{(4)})\sigma_{11} + 2\ \mathrm{Im}\left[\Omega_{12}^{(4)}\left(1 - \frac{i}{q_2^{(4)}}\right)\sigma_{21}\right], \quad (1)$$

$$\dot{\sigma}_{22} = -\Gamma_2\sigma_{22} - 2\ \mathrm{Im}\left[\Omega_{12}^{(4)}\left(1 + \frac{i}{q_2^{(4)}}\right)\sigma_{21} - \Omega_{23}^{(1)}\sigma_{32}\right], \quad (2)$$

$$\dot{\sigma}_{33} = -(\gamma_{3i}^{(1)} + \Gamma_3)\sigma_{33} - 2\ \mathrm{Im}[\Omega_{23}^{(1)}\sigma_{32}], \quad (3)$$

$$\dot{\sigma}_{21} = \left(i(\Delta_1 + S_1) - \frac{1}{2}(\gamma_{1i}^{(4)} + \gamma_{1b}^{(4)} + \Gamma_2)\right)\sigma_{21} - i\Omega_{12}^{(4)}\left[\left(1 - \frac{i}{q_2^{(4)}}\right)\sigma_{11} - \left(1 + \frac{i}{q_2^{(4)}}\right)\sigma_{22}\right] - i\Omega_{23}^{(1)}\sigma_{31}, \quad (4)$$

$$\dot{\sigma}_{31} = \left(i(\Delta_1 + S_1 + \Delta_2) - \frac{1}{2}(\gamma_{1i}^{(4)} + \gamma_{1b}^{(4)} + \gamma_{3i}^{(1)} + \Gamma_3)\right)\sigma_{31} + i\Omega_{12}^{(4)}\left(1 + \frac{i}{q_2^{(4)}}\right)\sigma_{32} - i\Omega_{23}^{(1)}\sigma_{21}, \quad (5)$$

$$\dot{\sigma}_{32} = \left(i\Delta_2 - \frac{1}{2}(\gamma_{3i}^{(1)} + \Gamma_3 + \Gamma_2)\right)\sigma_{32} + i\Omega_{12}^{(4)}\left(1 + \frac{i}{q_2^{(4)}}\right)\sigma_{31} - i\Omega_{23}^{(1)}(\sigma_{22} - \sigma_{33}), \quad (6)$$

$$\dot{\sigma}_{44} = (\gamma_{i1}^{(4)} + \gamma_{i1b}^{(4)})\sigma_{11} + \Gamma_2\sigma_{22} + (\Gamma_3 + \gamma_{3is}^{(1)})\sigma_{33} + 4\frac{\Omega_{12}^{(4)}}{q_2^{(4)}}\mathrm{Re}(\sigma_{21}) + \gamma_{5r}\sigma_{55} - R_s\sigma_{44}, \quad (7)$$

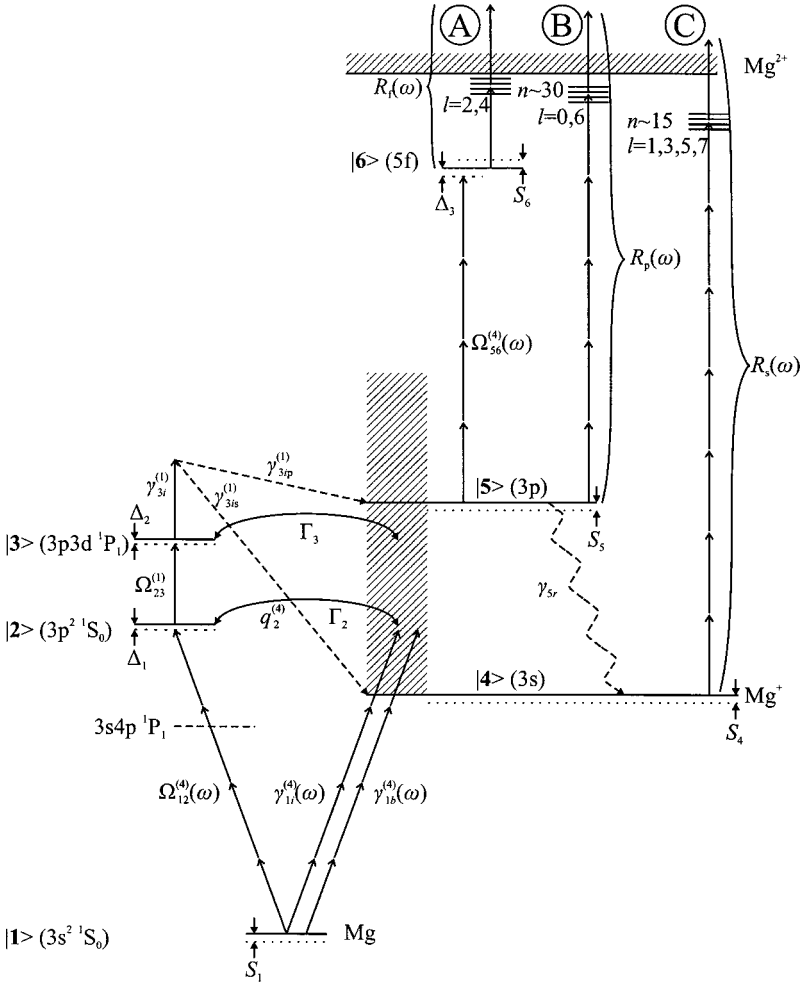

FIG. 2. Simplified energy level diagram of Mg (not to scale), depicting the atomic and ionic states and excitation parameters included in the theoretical model. The symbols are explained in the text.

$$\dot{\sigma}_{55} = \gamma_{3ip}^{(1)}\sigma_{33} - (\gamma_{5r} + R_p + \Omega_{56}^{(4)})\sigma_{55}, \tag{8}$$

$$\dot{\sigma}_{66} = \Omega_{56}^{(4)}\sigma_{55} - R_f\sigma_{66}. \tag{9}$$

Equations (1)–(6) are the density matrix equations governing the time evolution of Mg states $|1\rangle = |3s^2\ ^1S_0\rangle$, $|2\rangle = |3p^2\ ^1S_0\rangle$ and $|3\rangle = |3p3d\ ^1P_1\rangle$ under the action of the laser field whose intensity is given by $I(t) = I_{\max} f(t)$. The pulse envelope is assumed throughout the remaining of the paper to have the form $f(t) = \mathrm{sech}^2(1.76t/\tau_l)$, with $\tau_l = 5$ ns its FWHM, or equivalently the pulse duration. Equations (1)–(3) describe the time evolution of the populations of these states while the remaining three equations refer to the corresponding off-diagonal elements of the density matrix. States $|2\rangle$ and $|3\rangle$ are both autoionizing (AI), the former decaying to the degenerate $3s\varepsilon s\ ^1S_0$ continuum and the latter to the $3s\varepsilon s\ ^1P_1$ one. Their AI widths are denoted by Γ_2 and Γ_3, respectively (see also Fig. 2; their values are given in Table I). These resonances are represented as quasi-bound-states embedded in the adjacent degenerate continuum [12] and this representation leads naturally to the derivation of their positions, AI widths, Fano q-parameters and dipole couplings within the context of the density matrix formalism. This representation is also compatible with the configuration interaction (CI) approach employed for the calculation of these parameters. A brief description of this method will be given below. The ground state is coupled with four photons to the quasibound part of the $3p^2\ ^1S_0$ state, the coupling represented by the four-photon Rabi frequency $\Omega_{12}^{(4)}$. The excitation of the degenerate continuum $(3s\varepsilon s\ ^1S_0)$ is represented by $\gamma_{1i}^{(4)}$. The interference of the two excitation pathways is expressed by the four-photon Fano q-parameter $q_2^{(4)}$. The definition of all three parameters is a straightforward generalization of the corresponding two-photon ones given in Ref. [13]. These atomic parameters are constrained by the well-known relation $q_2^{(4)} = 2\Omega_{12}^{(4)}(\Gamma_2\gamma_{1i}^{(4)})^{-1/2}$. An additional four-photon decay to the background $3s\varepsilon d\ ^1D_2$ continuum is denoted by $\gamma_{1b}^{(4)}$. The bound state $3s4p\ ^1P_1$ is in near three-photon resonance throughout the wavelength range scanned in our experiment (584–596 nm) with a minimum detuning of approximately 1000 cm^{-1}. While, under our moderate laser intensities, this state is not populated, it nevertheless, incurs non-negligible wavelength dependence to all four-photon excitation probabilities from the ground state. Thus, we have calculated these four-photon dipole couplings for five values of the wavelength within the scanned range (given, together with the calculated couplings, in Table I) and linearly interpolated in between them to obtain smoothly varying, wavelength dependent couplings throughout the scanned range of wavelengths. This approach has already been successfully employed in an earlier study of the same system, albeit with a

TABLE I. Calculated Mg parameters used in the density matrix model [Eqs. (1)–(6)]. The intensity I is expressed in W/cm^2 and shifts, Rabi frequencies and ionization widths in rad/s.

			Mg			
S_1	Γ_2	Γ_3	$\Omega_{23}^{(1)}$	$\gamma_{3i}^{(1)}$	$\gamma_{3is}^{(1)}$	$\gamma_{3ip}^{(1)}$
$-25.3I$	5.4×10^{13}	3.8×10^{12}	$77.6I^{1/2}$	$27.673I$	$3\times10^{-3}I$	$27.670I$
λ (nm)	$\Omega_{12}^{(4)}/I^2$	$\gamma_{1i}^{(4)}/I^4$	$\gamma_{1b}^{(4)}/I^4$			
584.5	4.0×10^{-13}	3.7×10^{-40}	5.1×10^{-39}			
587.5	5.4×10^{-13}	6.2×10^{-40}	7.1×10^{-39}			
590.0	6.6×10^{-13}	8.9×10^{-40}	1.0×10^{-38}			
592.5	6.6×10^{-13}	2.2×10^{-39}	1.5×10^{-38}			
595.0	9.4×10^{-13}	3.8×10^{-39}	2.6×10^{-38}			

somewhat different excitation scheme [13]. The detuning from exact four-photon resonance is denoted by $\Delta_1=4\omega-(\omega_2-\omega_1)$, where ω_1 and ω_2 are the field-free energy positions of states $|1\rangle$ and $|2\rangle$, respectively. The small negative AC Stark shift of the ground state, S_1, has also been taken into account, its numerical value given in Table I. States $|2\rangle$ and $|3\rangle$ are coupled by a one-photon transition and the corresponding detuning is $\Delta_2=\omega-(\omega_3-\omega_2)$. Since $|3\rangle$ is very narrow (its AI width being approximately 25 cm^{-1}, see also Table I) it has been treated as a bound state as far as its dipole coupling to state $|2\rangle$ is concerned, which means we have neglected any continuum-continuum coupling between the two states [13]. Nevertheless, its AI width has been included as a decay channel contributing to the $Mg^+(3s)$ ion production. Additional one photon absorption from $|3\rangle$ has also been included through the total ionization width $\gamma_{3i}^{(1)}$. This width results from the sum of two contributions: $\gamma_{3is}^{(1)}$, the ionization width to the $3s\varepsilon l\ ^1S_0$ and $^1D_2$ continua and $\gamma_{3ip}^{(1)}$, the ionization width to $3p\varepsilon l\ ^1S_0$ and $^1D_2$ ones. All symmetry allowed continuum channels have been included in the calculations. As can be inferred from the values quoted in Table I, the ionization to the $3p\varepsilon l$ continua is the dominant laser induced decay mechanism from state $|3\rangle$. Moreover, for the highest intensities employed in the experiments, this radiative decay competes with the autoionization decay of state $|3\rangle$. The excitation-decay pathway from $|2\rangle$ to the $3p\varepsilon l$ continua via state $|3\rangle$ entails the enhanced absorption of two photons above the first ionization threshold and is the sole source of population for the Mg^+ $3p$ excited state. This is of critical importance for the production of Mg^{2+}, as will be analyzed in the following paragraphs. It should also be noted that the laser-induced shifts of states $|2\rangle$ and $|3\rangle$ from their field-free positions are dictated by their one-photon coupling and are not necessarily identical to AC Stark shifts or the ponderomotive shift.

Equations (7)–(9) describe, within a rate equations model, the time evolution of the multiphoton excitation in the Mg^+ ion and its subsequent ionization to produce Mg^{2+}. The ionic states explicitly included in the model are $|4\rangle=|3s\rangle$, $|5\rangle=|3p\rangle$, and $|6\rangle=|5f\rangle$. The first three terms on the right-hand side of Eq. (7) and the first term on the right-hand side of Eq. (8) are the source terms for the populations of the $3s$ and $3p$ ionic states, respectively, including all the autoionization and radiative decay mechanisms of the neutral atom that produce Mg ions in either of these states. The spontaneous decay of the $3p$ to the $3s$ has also been taken into account through γ_{5r} [14]. Within the rate equations model, which was adopted in order to simplify the description of the complicated multiphoton dynamics in the Mg ion and render it computationally manageable, we have defined three excitation-ionization pathways labeled, respectively, with A, B, and C (see Fig. 2 for a detailed graphical depiction of all three of them). Pathway C corresponds to the decay of the ground ionic state, $3s$, by seven-photon near-resonant, eight-photon ionization. The corresponding rate is defined as

$$R_s(\omega)=\sum_{n''l''}[\Omega_{s\to n''l''}^{(7)}(\Delta_{s\to n''l''}=0)]^2\frac{\frac{1}{2}\gamma_{n''l''}^{(1)}}{(\Delta_{s\to n''l''}+S_4-S_{\mathrm{pont}})^2+\frac{1}{4}(\gamma_{n''l''}^{(1)})^2} \tag{10}$$

and enters as the last term on the right-hand side of Eq. (7). It is the sum of 20 terms, each one having the typical form of the excitation rate from a bound initial state (the $3s$, in the present case) to an AC Stark shifting and ionizing final state (anyone from the set of 20, denoted by $n''l''$) [15]. The parameters needed to define the rate are the seven-photon Rabi frequency $\Omega_{s\to n''l''}^{(7)}(\Delta_{s\to n''l''}=0)$ to state $n''l''$, the ionization width, $\gamma_{n''l''}^{(1)}$, and the ponderomotive shift, S_{pond}, of this state, its detuning from seven-photon resonance, $\Delta_{s\to n''l''}=7\omega-(\omega_{n''l''}-\omega_{3s})$, and the AC Stark shift S_4, of the $3s$. The calculated values of these parameters (with the exception of the ponderomotive shift) are given in Table II. The theoretical methods employed for the calculation of these parameters will be presented at the end of this section. The ponderomotive shift is the same for all the high-lying $n''l''$ $(12<n''<16,\ l''=1,3,5,7)$ Rydberg states included in the calculation of the rate R_s [8]. These states have been chosen because, for the wavelengths and intensities employed in the experiments, they shift in and out of seven-photon resonance during the laser pulse and are therefore considered to be the ones mostly contributing to the double ion signal. In applying this state-selection criterion, the AC Stark shift of the $3s$

TABLE II. Calculated Mg^+ parameters used in the rate equation model [Eqs. (7)–(9)]. The intensity I is expressed in W/cm^2 and shifts, Rabi frequencies radiative and ionization rates in rad/s.

			Mg^+				
S_4	S_5	$S_6(\omega)$[a]	$\Omega_{56}^{(4)}(\Delta_3=0)$	γ_{5r}[b]			
$-79.0I$	$-10.3I$	$259.7I \leftrightarrow -3.2I$	$-28.8\times10^{-13}I^2$	2.857×10^8			
			$R_s(\omega)$			$R_f(\omega)$	
λ (nm)	R_p/I^4[c]	$n''l''$[d]	$\Omega_{s\to n''l''}^{(7)}(\Delta_{s\to n''l''}=0)/I^{7/2}$	$\gamma_{n''l''}^{(1)}/I$	$n'l'$[d]	$\Omega_{f\to n'l'}^{(1)}(\Delta_{f\to n'l'}=0)/I^{1/2}$	$\gamma_{n'l'}^{(1)}/I$
584.5	2.0×10^{-38}	$12p$	-2.7×10^{-33}	3.79	24d	3.7×10^6	0.78
587.5	1.2×10^{-38}	$12f$	1.0×10^{-33}	4.54	24g	10.3×10^6	0.32
590.0	3.4×10^{-39}	$12h$	-1.2×10^{-33}	1.15	25d	-3.5×10^6	0.69
592.5	1.9×10^{-39}	$12k$	-7.3×10^{-36}	8.02	25g	-9.0×10^6	0.28
595.0	4.5×10^{-40}	$13p$	2.8×10^{-33}	2.90	26d	3.2×10^6	0.61
		$13f$	1.2×10^{-33}	3.54	26g	7.9×10^6	0.25
		$13h$	1.3×10^{-33}	9.17	27d	-3.0×10^6	0.55
		$13k$	7.1×10^{-36}	7.03	27g	-7.0×10^6	0.22
		$14p$	-3.0×10^{-33}	2.24	28d	2.9×10^6	0.49
		$14f$	-1.5×10^{-33}	2.84	28g	6.1×10^6	0.20
		$14h$	1.0×10^{-33}	0.74	29d	-2.7×10^6	0.44
		$14k$	-6.9×10^{-36}	0.06	29g	-5.3×10^6	0.18
		$15p$	3.0×10^{-33}	1.84	30d	2.6×10^6	0.40
		$15f$	1.8×10^{-33}	2.30	30g	4.6×10^6	0.16
		$15h$	6.8×10^{-34}	0.61			
		$15k$	6.6×10^{-36}	0.05			
		$16p$	-3.6×10^{-33}	1.50			
		$16f$	-2.19×10^{-33}	1.89			
		$16h$	-7.0×10^{-34}	0.50			
		$16k$	6.3×10^{-36}	0.05			

[a]The maximum and minimum values are given. $S_6(\omega)$ is calculated at 10 different wavelengths within the range 584.5–595.0 nm.
[b]Calculated from the experimental lifetime measurements [14].
[c]Calculated for $n=18$, 24, 52 ($l=0$) and $n=17$, 23, 51 ($l=6$) states corresponding to resonant excitation [Eq. (11)] at 595, 590, and 585 nm, respectively.
[d]Experimental energy level positions are taken from Ref. [19].

ground ionic state and the ponderomotive shift of the Rydberg states have both been taken into account.

Pathways B and A, both start from the excited ionic state Mg^+ $3p$. Pathway B is a five-photon near-resonant six-photon ionization process while pathway A is a four-photon resonant two-photon ionization process that proceeds via the $5f$ (four-photon resonant) and a set of Rydberg states one-photon near resonantly excited from the $5f$. For the calculation of rate $R_p(\omega)$ (corresponding to pathway B) we have chosen a number of states of symmetry $l=0,6$ (given in footnote c of Table II) that are accessible by five photons from the $3p$ and are shifting through five-photon resonance around the peak intensity of the pulse for the higher end of the intensities employed in the experiment ($\sim 9\times10^{11}$ W/cm^2). The expression for this rate is

$$R_p(\omega) = 2\sum_{nl} \frac{[\Omega_{p\to nl}^{(5)}(\omega)]^2}{\gamma_{nl}}. \tag{11}$$

At different wavelengths in the experimentally scanned range, vastly different parts of the corresponding Rydberg series are fulfilling the resonance condition rendering a detailed calculation particularly cumbersome. We have thus limited our calculations to five specific values of the wavelength (also given in Table II) and the corresponding states are interpolated linearly between these values of $R_p(\omega)$ to obtain its values at a desired wavelength mesh that was subsequently used in the time-dependent calculation. This wavelength-dependent excitation rate should be considered as an averaged quantity that takes into account the most significant contributions to double ion production through pathway B. Pathway A, is modeled in two steps. First, the $5f$ is near-resonantly excited from $3p$ at a rate given by the following expression:

$$\Omega_{56}^{(4)}(\omega) = [\Omega_{56}^{(4)}(\Delta_3=0)]^2 \frac{\frac{1}{2}R_f(\omega)}{[\Delta_3 + S_5 - S_6(\omega)]^2 + \frac{1}{4}[R_f(\omega)]^2}, \tag{12}$$

where $\Omega_{56}^{(4)}(\Delta_3=0)$ is the resonant four-photon Rabi frequency from $3p$ to $5f$ (given in Table II), $\Delta_3=4\omega-(\omega_{5f}$

$-\omega_{3p}$) is the field-free four-photon detuning from resonance and S_5, S_6 are the AC Stark shifts of the $3p$ and $5f$, respectively. The calculation of S_5 is straightforward and is performed by applying the usual definition of this quantity (see, for example, the appendix in Ref. [8]) at $\lambda=590$ nm (in the middle of the scanned range) because it is very weakly wavelength dependent. The calculation of S_6 is more complicated. This laser-induced shift is dominated by the one-photon near-resonant coupling of $5f$ to Rydberg states $n'l'$ ($24<n'<30$, $l'=2,4$). Since these states have been only indirectly included in the dynamics of the ion, through their contribution to the effective two-photon ionization rate R_f, in order to take into account their contribution to the laser-induced shifting of $5f$ we have calculated S_6 as an AC Stark shift for 10 equidistant values of the wavelength spanning the range from 585 nm to 595 nm. In this way, a strongly wavelength-dependent quantity was obtained (as can be inferred from its extreme values given in Table II) and subsequently used in the rate equations system. The ionization rate of $5f$ through a near one-photon resonant two-photon process is given by

$$R_f(\omega)=\sum_{n'l'}[\Omega^{(1)}_{f\to n'l'}(\Delta_{f\to n'l'}=0)]^2 \times\frac{\frac{1}{2}\gamma^{(1)}_{n'l'}}{[\Delta_{f\to n'l'}+S_6(\omega)-S_{\mathrm{pont}}]^2+\frac{1}{4}(\gamma^{(1)}_{n'l'})^2}, \quad (13)$$

where $\Omega^{(1)}_{f\to n'l'}(\Delta_{f\to n'l'}=0)$ is the one-photon Rabi frequency from the $5f$ to the $n'l'$ Rydberg state, $\Delta_{f\to n'l'}=\omega-(\omega_{n'l'}-\omega_{5f})$ is the corresponding detuning, and $\gamma^{(1)}_{n'l'}$ is the ionization width of the $n'l'$ Rydberg state. The labels of these states and the values of the corresponding parameters are given in Table II. The states included in the calculation are those that are ponderomotively shifted through one-photon resonance with the shifted $5f$ position, during the laser pulse. These remarks conclude the presentation of the system of dynamic equations.

For each wavelength, Eqs. (1)–(9) are simultaneously integrated from $t_{\mathrm{in}}=-2\tau_l$ to $t_{\mathrm{fin}}=2\tau_l$ with the peak of the laser pulse corresponding to $t=0$. The numerical technique employed for the integration of the system of equations is an embedded fifth-order Runge-Kutta method with adaptive step size control [16]. The calculations were carried out on a commercial personal computer. The solution of the system (i.e., the values of σ_{ij}, $i,j=1,3$ and σ_{kk}, $k=4,5,6$ as functions of time for a specific wavelength and peak laser intensity) are used for the calculation of observable quantities that are directly compared to the experimental data. Specifically, the total Mg^+ signal is calculated as $N_+=(\sigma_{22}+\sigma_{33}+\sigma_{44}+\sigma_{55}+\sigma_{66})_{t\to\infty}$, i.e., as the sum of the populations in the AI states and the populations left in the three ionic states at the end of the pulse. The long-time limit implies that all the population in the AI states will rapidly decay after the end of the pulse and will be collected as Mg^+ signal. Similarly, any redistribution of population between the ionic states, because of the spontaneous decay of the excited ones to the ground state, will not affect the recorded singly charged ion signal. The doubly charged ion yield is calculated as $N_{2+}=1-N_+-(\sigma_{11})_{t\to\infty}$, or alternatively and equivalently as $N_{2+}=N^s_{2+}+N^p_{2+}+N^f_{2+}$. The former equality results from the obvious assumption that within our sequential excitation model the system is closed and at the end of the pulse whatever population has not ionized (either singly or doubly charged) will remain in the ground state. The latter expression rests on the reasonable assumption that at the experimental intensities for which double ion production is recorded the one-photon ionization from the final set of Rydberg states involved in pathways A, B, and C is saturated and therefore once the system is excited in the vicinity of these Rydberg states is certainly ionized. Therefore, the contribution of each of the three pathways to the double ion yield can be expressed as

$$N^f_{2+}=\int_{\Delta t}R_f\sigma_{66}\,dt, \quad N^p_{2+}=\int_{\Delta t}R_p\sigma_{55}\,dt,$$

$$N^s_{2+}=\int_{\Delta t}R_s\sigma_{44}\,dt.$$

The integration extends over the same time interval as the solution of the set of dynamical equations. Both expressions for the calculation of the double ion yield have been used and their equivalence within our model has been numerically verified. Finally, the fluorescence yield from the excited $3p$ towards the $3s$ ground state, that has been used as an experimental probe of the population of $3p$, has been calculated as $N_{\mathrm{fluo}}=\int_{\Delta t}\gamma_{5r}\sigma_{55}\,dt$.

Before closing the theory section it is necessary to give some details about the array of techniques we have employed for the calculation of the atomic parameters, i.e., the parameters entered in the set of dynamic equations, that we collectively call them atomic although they refer to both the Mg atom and its ion, Mg^+. We treat atomic Mg as a two-valence electron system outside a frozen, doubly charged ionic core [13]. This core is described within the self-consistent field approximation. Then a one-electron Hamiltonian is built by taking into account the interaction of a single electron with the frozen core including core polarization effects through an appropriately parametrized potential [13]. This Hamiltonian is diagonalized on a *B*-spline basis set that includes 350 *B*-splines (of order 10) per angular momentum confined in a radial box of 150 a.u. and defined over a linear mesh. The cutoff parameters of the core polarization potentials are optimized in order to reproduce the lower excited states of Mg^+ of each symmetry ($l=0-5$). The one-electron orbitals are orthogonalized to the core wave functions and are, subsequently, combined to build properly antisymmetrized two-electron configurations. The two-electron states of specific symmetry are obtained by diagonalizing the two-electron Hamiltonian, which includes an appropriately parametrized dielectronic polarization potential, within the corresponding space of configurations (configuration interaction calculation, CI). The calculation of bound states or unstructured continua is straightforward. The AI resonances are described as isolated quasibound states embedded in a degenerate continuum within the framework of the Feshbach formalism [13], implemented by partitioning the configuration space in

two subspaces, usually denoted by Q and P, that are coupled only by the electron-electron interaction, i.e., the part of the two-electron Hamiltonian responsible for the configuration mixing. In a typical CI calculation for bound states or for the quasibound component of an AI state between 400 and 500 configurations are included. The representation of the discretized continua is satisfactory with approximately 100 to 200 configurations. Our results for the positions of bound and AI states as well as the widths of the autoionizing states agree reasonably well with earlier theoretical and experimental results [13]. The various dipole couplings, and in particular the multiphoton ones, have been obtained by using the calculated two-electron wave functions and a Green's function technique to perform the summation over intermediate states [17,13]. In order to facilitate the comparison with the experimentally recorded spectra we have used the experimental value for the energy of the $3s^2$ Mg ground state in the calculation of the energy denominators in the multiphoton matrix elements [17]. The dipole operator in both the length and the velocity gauge has been used in the calculations of the dipole couplings. As a general rule, the agreement between the results obtained with the two different representations is usually in the order of 15% or better. A notable exception is $\gamma_{1b}^{(4)}$, the four-photon ionization width from the ground state to the $3s\varepsilon d\ ^1D_2$ continuum, for which the two results differ substantially. We have used the value obtained in the velocity gauge (quoted in Table II), since it turned out to have converged with respect to the box length and the size of the basis set.

The parameters for the Mg^+ have been obtained within the framework of single channel quantum defect theory (SQDT), an approach used successfully over the years for the theoretical description of time-dependent multiphoton processes in one-active electron systems [18]. By exploiting the extensive tables of bound state energies for Mg^+, provided online by NIST [19], we have obtained weakly energy dependent quantum defect parameters for all Rydberg series of interest for the simulation of the ionic dynamics. In this way the energy positions of very high-lying states ($n>20$) are predicted with satisfactory accuracy. Moreover, by smoothly extrapolating these parameters above the first ionization threshold of Mg^+ it is possible to obtain energy normalized continuum wave functions that are employed to evaluate ionization cross sections. The notoriously difficult calculation of multiphoton dipole couplings for high order transitions (orders 4, 5, and 7 in our case) is performed by employing a numerically efficient method [20] that converts a recurrence relation satisfied by the multiphoton matrix elements into a set of complex linear first-order differential equations. For one-photon bound-bound and bound-free matrix elements we have employed the techniques developed in Ref. [21] that are numerically efficient and reasonably accurate even when, as in our case, high-lying Rydberg states are involved. All calculated matrix elements have been properly Z scaled [22], since, within the context of SQDT, Mg^+ is treated as a hydrogenic system with $Z=2$. The length representation of the dipole operator has been used in all SQDT calculations and the radial range of the integration was taken sufficiently long (typically 100 a.u.) for the results to be converged.

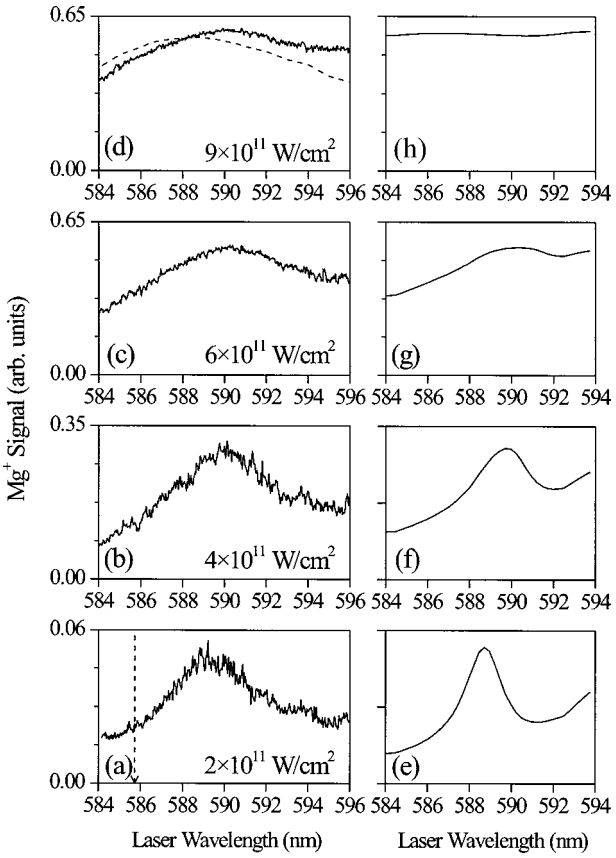

FIG. 3. Experimental (a)–(d) and corresponding theoretical (e)–(h) Mg^+ spectra for different laser intensities. The vertical dashed line in (a) marks the wavelength of the unperturbed $3s^2\ ^1S_0$-4ω-$3p^2\ ^1S_0$ resonance. In (d) the dye profile is drawn with dashed line.

IV. RESULTS AND DISCUSSION

A. The Mg^+ yield

The Mg^+ yield as a function of laser wavelength near the $3s^2\ ^1S_0$-4ω-$3p^2\ ^1S_0$ transition is shown in Figs. 3(a)–3(d) for four different laser intensities. The spectrum in Fig. 3(a) is recorded with a relatively low intensity, while that in Fig. 3(d) with the maximum obtainable one. The vertical dashed line in Fig. 3(a) marks the unperturbed resonance position (68 275 cm^{-1}, $\lambda \approx 585.7$ nm) of $3p^2\ ^1S_0$, according to the available spectroscopic data [19,23] and additional measurements of ours acquired by low-intensity, two-photon ionization experiments. It is evident that the resonance peak position is considerably shifted with respect to its unperturbed location even for the lowest intensity shown ($\sim 2 \times 10^{11}$ W/cm^2). As the power density increases above $\sim 5 \times 10^{11}$ W/cm^2, this shift attains its maximum value. For the highest intensities, the resonant and nonresonant contributions to the signal become comparable leading to an apparent broadening of the resonance and finally to an almost unstructured ion spectrum, a clear sign of saturation. It is also noticeable that the background is always higher on the red side of the resonance, despite the lower laser pulse energy output of the dye solution in this wavelength range [Fig. 3(d)]. This

fact is attributed to the tail of the four-photon ionization process from the $3s^2\ ^1S_0$ ground state via the three-photon near-resonant transition to the bound $3s4p\ ^1P_1$ level (see Fig. 2). The exact position of that resonance (49 346.7 cm^{-1}, $\lambda \sim 607.8$ nm), does not fall within the scanned wavelength range. If AC-Stark shift effects are ignored, the smallest three-photon detuning within this range is quite large ($\sim$1000 cm^{-1}). Yet it is known that this transition is very strong [24] and at high intensities its tail affects the ion spectra even far away from the resonance. The shape of the background signal and the large shift of the $3s^2\ ^1S_0$-$3p^2\ ^1S_0$ four-photon transition observed in the present study are in close agreement with the electron energy analysis experiment of van Druten *et al.* [8], performed mainly with 1 ps laser pulses. In addition, this behavior is satisfactorily predicted by the theoretical model presented earlier. As it can be seen in Figs. 3(e)–3(h) the large shift of the $3p^2\ ^1S_0$ level, attributed to its strong radiative coupling with the $3p3d\ ^1P_1$ autoionizing state, is accurately reproduced for all the intensities. On the contrary, the resonant width is reproduced only for the highest ones. The reason for this small discrepancy is not clear as yet. Moreover, at low intensity the model overestimates the higher red side background ionization signal although the $3s^2\ ^1S_0$-3ω-$3s4p\ ^1P_1$ resonance is only implicitly taken into account through the frequency dependence of the four-photon Rabi frequency $\Omega_{12}^{(4)}$ and ground state ionization widths $\gamma_{1i}^{(4)}$ and $\gamma_{1b}^{(4)}$. The largest contribution to the tail is found to stem from the background ionization width $\gamma_{1b}^{(4)}$ to the $3s\varepsilon d\ ^1D_2$ continuum, for which the velocity gauge result is employed in the model. On the other hand, as the intensity increases the theoretical and experimental Mg^+ yield spectra look much more similar, despite the fact that the dye profile is not introduced in the calculation. At the highest intensity the model predicts complete saturation accompanied with a small drop of the Mg^+ signal (around 591 nm), attributed to Mg^{2+} formation. In conclusion, the energy-dependent background ionization signal, saturation effects and Mg^{2+} creation are found to be responsible for the fact that the shift of the $3p^2\ ^1S_0$ resonance is apparently fixed at high intensity.

Typical recordings of the Mg^+ signal as a function of laser power density are shown in the log-log plots of Figs. 4(a) and 4(b) for two selected laser wavelengths, 592 nm and 588 nm, respectively. The latter wavelength is close to the unperturbed position of the $3p^2\ ^1S_0$ resonance while the former lies near its location at the highest intensities available in the present study. The data shown in Fig. 4(a) have been recorded with an $f=10$ cm focal length lens while those of Fig. 4(b) with an $f=15$ cm one. Power law I^{K_+} fits to the unsaturated parts of the experimental curves produce for all wavelengths an order of nonlinearity $K_+ \approx 4$ (for the data shown the fitted values are $K_+=4.09\pm0.03$ for 592 nm and $K_+=3.98\pm0.03$ for 588 nm). That is to be expected for a four-photon ionization process and the gradual shift of the resonance with increasing intensity does not seem to produce a wavelength dependent order of nonlinearity. This fact is in perfect agreement with theoretical predictions. The saturated part of the plots is not parallel to the x axis but, rather, the ionic signal continues to increase with a lower slope. This well-known phenomenon is due to the increase of the focal

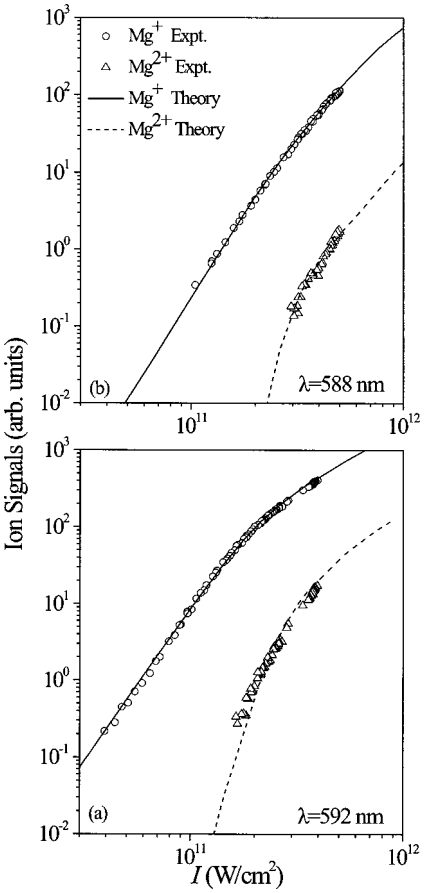

FIG. 4. Experimental and theoretical singly and doubly charged ion yields as a function of laser intensity. (a) Laser wavelength 592 nm; focusing lens focal length $f=10$ cm. (b) Laser wavelength 588 nm; focusing lens focal length $f=15$ cm. Typical y axis uncertainties are of the order of the symbols size. For more details see text.

volume as the intensity increases and for Gaussian beams the slope of the saturated part is equal to 3/2 (see, for example, Ref. [25]). In order for the theory to reproduce this effect it is found necessary to spatially integrate the calculated Mg^+ yield, N_+ (as well as the Mg^{2+} yield, N_{2+}) over the interaction volume. This procedure does not affect the order of nonlinearity of the unsaturated part. The spatially integrated ionic populations are then given by

$$\langle N \rangle_{r,z} \propto \int_0^{I_{\max}} N(I) K(I, I_{\max}) dI, \tag{14}$$

where the function

$$K(I, I_{\max}) \equiv \frac{dV(I, I_{\max})}{dI} = \frac{2I + I_{\max}}{I^2} \left(\frac{I_{\max} - I}{I} \right)^{1/2} \tag{15}$$

applies strictly only for Gaussian laser beams [26]. The curves computed through Eqs. (14) and (15) fit both the saturated and unsaturated part of the plots. Matching theoretical to experimental values requires, of course, an appropriate scaling for the y axis (signal). Concerning the x axis, no scaling of the theoretical intensity values is practically re-

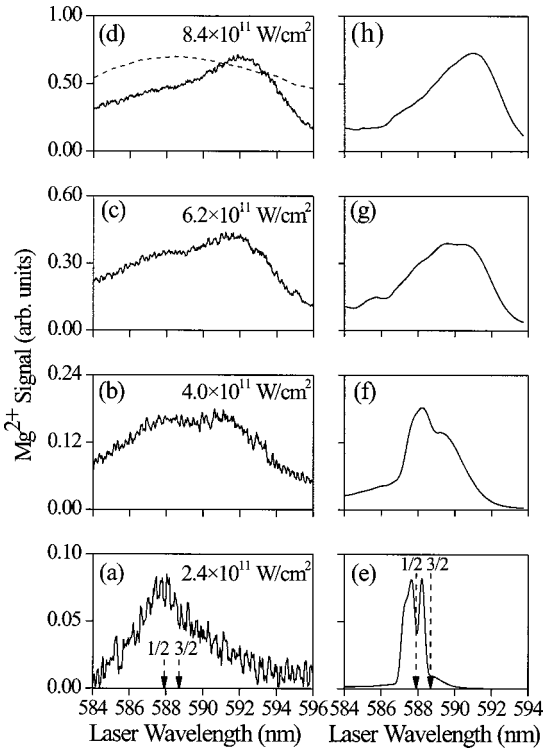

FIG. 5. Experimental (a)–(d) and corresponding theoretical (e)–(h) Mg^{2+} spectra for different laser intensities. The vertical dashed lines in (a) and (e) mark the wavelengths of the unperturbed $3p_{1/2,3/2}$-4ω-$5f_j$ Mg^+ resonances. In (d) the dye profile is drawn with dashed line.

quired for the data recorded with the $f=15$ cm focal length lens, apart from the unavoidable factor translating peak to average pulse intensities (for the assumed pulse shape they are related by $\bar{I}\approx 1.13 I_{\max}$). On the contrary, for the data recorded with the $f=10$ cm focal length lens [such as those shown in Fig. 4(a)] the overall scaling factor was found to be 2.8. In other words, the theoretically predicted saturation intensity is found to be $\sim$2.8 times higher than the experimental one. Scaling parameters of similar magnitude are not unusual in multiphoton ionization studies [10,13]. However, since no scaling is required for the data recorded with the longer focal length lens we conclude that our finding under tighter focusing conditions may be attributed to space charge effects. Their importance would be greater when short focal length lenses are used since this leads to the production of higher ionic populations within a smaller volume. The above assumption is also supported by earlier experimental and theoretical studies where it was demonstrated that under space charge conditions the order of nonlinearity is not affected but the apparent saturation intensity decreases [27]. In that case, however, the atomic density employed was much higher ($\sim 10^{11}$ cm^{-3}) and the saturation intensity decreased by about a factor of ten with respect to the expected value.

B. The Mg^{2+} yield

Figures 5(a)–5(d) assemble typical plots of the Mg^{2+} yield as a function of laser wavelength, recorded simultaneously with the Mg^+ signal. The spectrum of Fig. 5(a) is recorded with nearly the lowest intensity for which Mg^{2+} ions are detectable under our conditions, while Fig. 5(d) with the maximum available one. It is evident from the plots that most of the spectra exhibit asymmetric profiles. However, the long tail of the low intensity recording of Fig. 5(a) lies on the red side of the spectrum and the maximum signal appears around 588 nm. As the intensity increases the asymmetry is gradually reversed and the signal's maximum appears finally at $\sim$592 nm. For intermediate power densities the shape of the spectra is that of two partly merged lobes. Apparently, Mg^{2+} ions are produced by two competing mechanisms each of which dominates at different intensities. In a first attempt to identify those mechanisms, we note that for the lowest intensity the spectral maximum is slightly blueshifted with respect to the four-photon $3p_{1/2,3/2}$-$5f_{5/2,7/2}$ ionic transitions. Considering our resolution and the number of photons required for this ionization path (six in total—see pathway A in Fig. 2) only two lines are expected to show up (the $5f_j$ level fine structure amounts to 0.06 cm^{-1} [19]). The unperturbed locations of these lines (the first for the $3p_{1/2}$ initial state and the second for the $3p_{3/2}$ one) are marked by the vertical arrows in Fig. 5(a). Experimentally only one line is observable. This fact might be attributed to the proximity of the fifth absorbed photon to a manifold of highly excited ionic Rydberg states ($n\sim 30$), which could broaden and merge by the DC field used to extract the ions in our TOF apparatus. Nevertheless, this scenario suggests that excited Mg^+ ions are formed into the $3p_{1/2,3/2}$ levels, which in turn implies the absorption of two photons above the Mg atom's first ionization threshold. Indeed, the excited state ionic populations are successfully probed by the fluorescence study presented in the next section. The other mechanism though, responsible for double ionization at high intensities, cannot be unambiguously determined solely from the analysis of experimental spectra and it is at this point that assistance from theoretical calculations becomes decisive. Figures 5(e)–5(h) show the computed Mg^{2+} spectra. At the lowest intensity a satisfactory agreement between the experimental spectrum and the envelope of the calculated one is found. Since theory does not include the aforementioned DC field present in the experiment, a few distinct resonances appear in Fig. 5(e). They are assigned to one-photon resonant two-photon ionization processes of the ionic Mg^+ $5f$ level through the manifold of Rydberg states with $24\leqslant n\leqslant 30$ and l restricted to d and g levels (pathway A in Fig. 2). Additionally, a weak and broad peak on the red side of those resonances is observable and it is responsible for the asymmetry of the spectral envelope. That peak stems from the five-photon resonant six-photon ionization of $3p$ levels through a different manifold of Rydberg states with $24\leqslant n\leqslant 30$ and $l=0$ and 6 (pathway B in Fig. 2). States with these values of orbital angular momentum cannot be radiatively coupled by one photon to the Mg^+ $5f$ level. By increasing the intensity this path gains in importance and finally dominates. As it can be seen in Fig. 5(f) the calculated double ionization yield via the $3p$-4ω-$5f$ ionic transition is still the strongest at intermediate intensities and, consequently, theory predicts that the contribution from pathway B scales with intensity at a slower rate than that expected on the basis of experimental evidence. For the highest

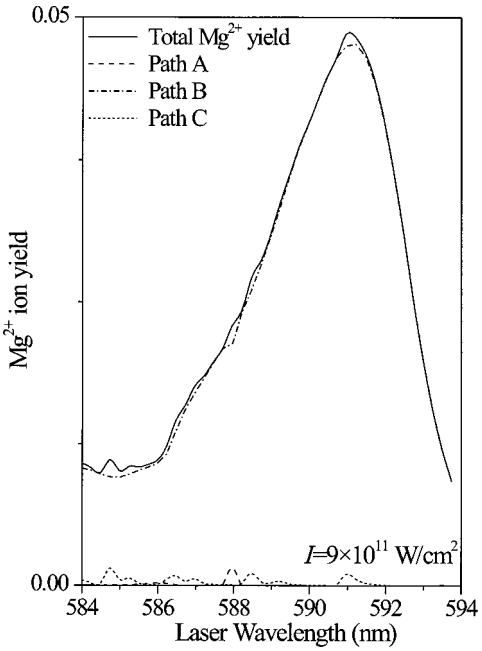

FIG. 6. Theoretical total and partial Mg^{2+} yield as a function of laser wavelength for the highest available experimental intensity. The total Mg^{2+} yield, N_{2+}, is normalized to unity. The total yield, N_{2+}, as well as the partial yields, N^s_{2+}, N^p_{2+}, N^f_{2+}, are calculated as described in Sec. III.

intensities however the produced spectrum compares well with experiment. Due to the approximations adopted in the calculation of the ionization rate through pathway B, distinct resonances are absent in this case. It is also noteworthy that pathway C in Fig. 2, i.e. the seven-photon resonant eight-photon ionization process out of the ionic Mg^+ $3s$ ground state, contributes only an insignificant fraction to the double ionization signal even for the highest intensity available in the present experiment. This is illustrated in Fig. 6 where the contributions of all three different pathways, A, B, and C, as well as the total double ionization yield are plotted for the maximum experimental intensity. Additional runs suggest that the ionic ground state ionization contributes significantly to the Mg^{2+} signal for intensities well above 10^{12} W/cm^2.

There is still an open question to be answered in order to complete the picture, namely why pathways A and B dominate at different intensities although they share the same initial level. To clarify this point, one has to follow the population accumulated to the Mg^+ $3p$ state as a function of wavelength and for different intensities. It turns out that this behavior is determined by the shift of the $3p^2\ ^1S_0$ state. For the lowest intensities, the population peaks around a wavelength range that falls near the Mg^+ $3p$-4ω-$5f$ resonance. Hence, pathway A dominates in this case. As the intensity increases, the maximum of the population is further pushed to lower wavelengths and pathway A can no more significantly contribute to doubly charged ion formation. Pathway B, on the other hand, has no specific wavelength dependence but it is expected to present a weaker overall ionization probability. Consequently, it becomes important at higher intensities and the fact that double ionization peaks at around 592 nm is simply related to the maximum of the Mg^+ $3p$ population also attained at this wavelength.

The picture described above is consistent with the measurements of Mg^{2+} yield vs power density shown in Figs. 4(a) and 4(b). Power law $I^{K_{2+}}$ fits to experimental data produce a slope $K_{2+}\sim 4.5$ for 588 nm (pathway A) and $K_{2+}\sim 5.1$ for 592 nm (pathway B). For all wavelengths larger than 589 nm, the slopes K_{2+} are found always greater than five (they range between 5.1 and 5.6 and typical uncertainties are of the order of ± 0.1). In fact the theoretical Mg^{2+} curves exhibit saturation at the power densities of interest and the experimentally determined slopes have little meaning apart from the demonstration that, as expected, the onset of doubly charged ion yield saturation occurs at lower intensities when pathway A dominates. Moreover, theory predicts that the observed saturation is due to both Mg and excited Mg^+ depletion within the interaction volume. Indeed, as is evident from Figs. 4(a) and 4(b), Mg^{2+} ions are detectable just at the onset of Mg^+ yield saturation. Note that in order to match theoretical and experimental Mg^{2+} curves in Figs. 4(a) and 4(b) the same x axis (laser intensity) scaling factors determined from the Mg^+ curves have been employed. In fact, even the y axis scaling factors are found practically the same with those for Mg^+ because the theoretical ratio N_{2+}/N_+ is for the highest intensities close to 5%. Considering the complexity of the model and the unaccounted for ion collection efficiency of our apparatus the predicted ratio agrees very well with the experimental value of 3–5%.

C. Experimental verification of excited Mg^+ ion formation: Fluorescence study

The present fluorescence study is undertaken in order to confirm the interpretation given earlier with experimental evidence and to investigate in more detail the strong radiative interaction between autoionizing states. In a first step, monochromator scans are performed over the whole range of operation of the UV-monochromator/solar-blind-PMT system (200–400 nm), for a number of fixed laser wavelengths. Within this range and for maximum sensitivity only two lines are observed corresponding to the $3p_{1/2,3/2}$-$3s_{1/2}$ Mg^+ transitions. A typical monochromator scan is shown in Fig. 7(a). This is a direct proof that excited $3p_{1/2,3/2}$ Mg^+ population is indeed created during the laser pulse. Since no evidence of other transitions is found the monochromator is replaced by a UV filter, simply to avoid stray visible laser light entering the PMT. Then, in a second step, the total unresolved fluorescence is recorded as a function of laser wavelength. In any of the two steps, the PMT signal is also recorded as a function of Mg density in order to rule out any collisionally induced effects stemming from the high atomic density (10^{14}–10^{16} cm^{-3}) in the cell. The dependence of the total fluorescence on atomic density is plotted in Fig. 7(b) together with a power law fit. The dependence is evidently linear, apart from the higher densities where the departure from linearity suggests the increasing importance of collisional phenomena. Therefore, all the reported measurements are obtained within the linear part of the curve in Fig. 7(b).

The total unresolved fluorescence as a function of laser wavelength is plotted in Figs. 8(a)–8(c) for a number of laser power densities. The significant red shift with respect to the

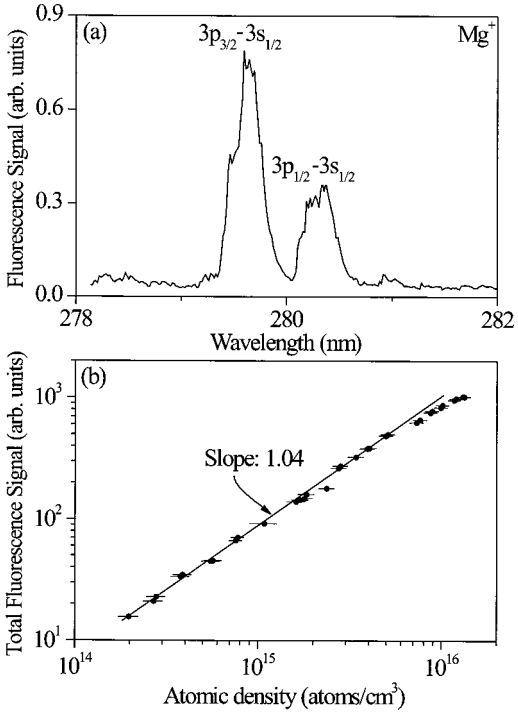

FIG. 7. (a) Typical monochromator scan near the $3p_{1/2,3/2}$-$3s_{1/2}$ Mg^+ decay transitions for fixed laser wavelength (590 nm) and intensity ($\sim 8\times 10^{11}$ W/cm^2). (b) Total fluorescence signal as a function of Mg vapor density. The solid line corresponds to a power law fit to the linear part of the plot.

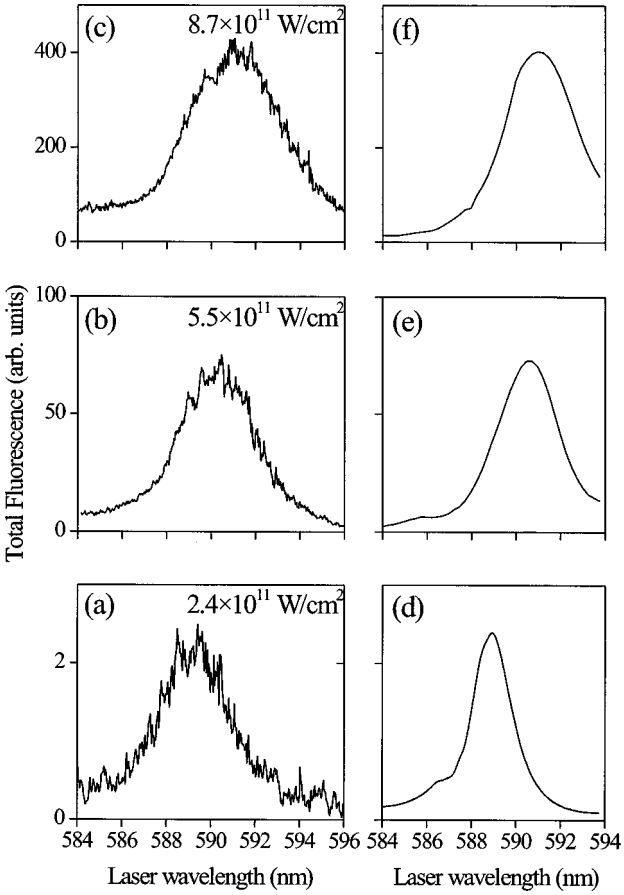

FIG. 8. Experimental (a)–(c) and corresponding theoretical (d)–(f) total fluorescence spectra as a function of laser wavelength for different intensities. Theoretical curves are calculated as described in Sec. III.

unperturbed position of the $3s^2\ ^1S_0$-4ω-$3p^2\ ^1S_0$ transition (expected at $\sim$585.7 nm) is quite evident (the highest value is more than twice the $\sim$280 cm^{-1} $3p^2\ ^1S_0$ state autoionization width). It is similar to that observed in the Mg^+ spectra. However, the observed shift is here somewhat larger for any given intensity and it saturates at higher values. One may also note the absence of any significant background signal. This is to be expected, since the ground state four-photon ionization cannot contribute to the excited Mg^+ production. Furthermore, the fluorescence profiles exhibit reversed (and much smaller) asymmetry with respect to the corresponding Mg^+ spectra. This behavior is accurately reproduced by the calculation [the relevant spectra are assembled in Figs. 8(d)–8(f)] although the profile widths are again rather underestimated by the model. The analysis of theoretical results uncovers some interesting aspects of the laser-Mg atom interaction in this energy range. In particular, it turns out that the observed two-photon absorption above the first Mg ionization threshold is clearly dictated by the strong one-photon coupling between the $3p^2\ ^1S_0$ and $3p3d\ ^1P_1$ doubly excited states, both acting as steps in a ladder leading to the $3p_{1/2,3/2}$ Mg^+ formation. This coupling was explored in various multilaser studies in the past, such as the studies of laser-modified autoionizing structures [13] and the three-autoionizing-states ladder schemes [28]. In our study, the wavelength of the unperturbed $3p^2\ ^1S_0$-$3p3d\ ^1P_1$ resonance position ($\sim$566.4 nm) is outside the scanned range. The shortest unperturbed detuning, approximately $\sim$530 cm^{-1} (for $\lambda_{laser}\sim$ 584 nm), is considered as large by conventional standards. However, it is (i) much smaller than the corresponding shortest one-photon detuning of the $3p^2\ ^1S_0$ state from the bound $3s4p\ ^1P_1$ level (only implicitly taken into account in our model) and (ii) small enough to lead to a coupling that can no longer be treated within perturbation theory. These findings may explain why absorption of two photons above threshold is made possible with long laser pulses of ns duration, a situation that is rather unexpected. They also point out very clearly to the important role played by autoionizing resonances in multiphoton single and double ionization processes of alkaline-earth-metal atoms.

A direct manifestation of the above-mentioned strong coupling is the fact that the observed shifts cannot be predicted in terms of perturbative AC Stark shift theory. The present calculations suggest that we are rather dealing with a situation analogous to the Rabi splitting of two resonantly coupled states, even more so since the $3p3d\ ^1P_1$ has been treated as a bound state, as far as its coupling to the $3p^2\ ^1S_0$ is concerned. Thus, what is experimentally observed is a fluorescence probe of the ionization from one of the two components into which this doubly excited state splits. The contribution of the other component lies outside the scanned wavelength range. The excitation cross section is nonzero at the unperturbed (zero field) position of the four-photon resonance, $\sim$585.7 nm, and this explains the reversed asymmetry of the fluorescence profiles when compared to the Mg^+ spec-

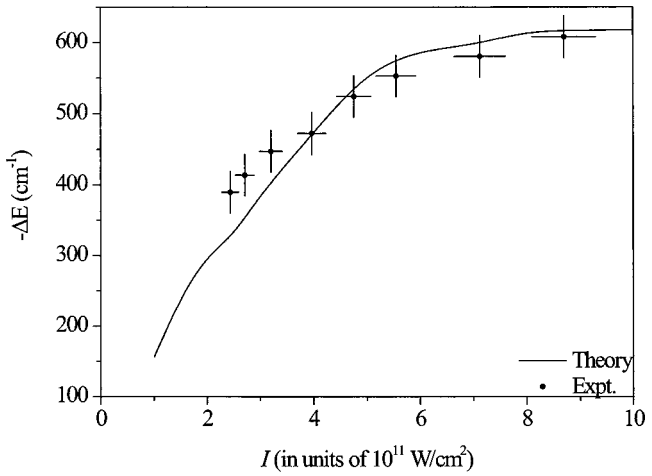

FIG. 9. Energy (four-photon) shift of the maximum of the total fluorescence spectra with respect to the unperturbed position of the $3p^2\ ^1S_0$ energy level as a function of laser intensity.

tra. Moreover, the shift is clearly a nonlinear function of the intensity as can be seen in Fig. 9.

It must be emphasized, however, that if the contribution of the bound $3s4p\ ^1P_1$ state to the four-photon excitation of the $3p^2\ ^1S_0$ is neglected, the departure from linearity is less significant and an accurate reproduction of the experimental data cannot be achieved. It is for this reason that our model takes this coupling into account in the implicit manner described earlier. It is also worth mentioning that if the background ionization width, $\gamma_{1b}^{(4)}$, is neglected, the agreement between theory and experiment is only qualitative. The quantitative agreement of Fig. 9 is obtained only after its value given in Table I is introduced in the model. A possible explanation for this result may be that at high intensities the background ionization competes with the resonant excitation of the $3p^2\ ^1S_0$ state and, therefore, prevents further atomic excitation and subsequent accumulation of population in the ionic $3p_{1/2,3/2}$ levels.

V. CONCLUSION

This work dealt with single and double ionization of magnesium with laser pulses of ns duration and moderate intensity ($<10^{12}$ W/cm^2). The experimentally and theoretically examined wavelength range between 584 nm and 596 nm includes the four-photon $3s^2\ ^1S_0$-$3p^2\ ^1S_0$ resonance. A broad peak corresponding to that resonance was found to be considerably redshifted with respect to its low-intensity position dominated the recorded Mg^+ spectra. This shift was the first out of many manifestations of the strong one-photon coupling between the $3p^2\ ^1S_0$ and $3p3d\ ^1P_1$ autoionizing states. This ladder excitation scheme within the continuum proved to be instrumental in inducing efficient excited ionic state production and subsequent double ionization. The excited $3p_{1/2,/3/2}$ Mg^+ state population was successfully probed by a fluorescence experiment and quite accurately predicted by our calculations based on a combination of density matrix and rate equations. The parameters entered in the dynamic equations to quantitatively describe laser-induced excitation and ionization in Mg and Mg^+ as well as AI in Mg were calculated independently using an array of well-established techniques. In general, and considering the complexity of the description of the atomic and ionic ionization process, theory and experiment were found to agree quantitatively. Hence, the mechanisms of sequential double ionization were clearly identified. The Mg^{2+} ions originate either through the four-photon $3p_j$-$5f_{j'}$ ionic transitions or the five-photon resonant six-photon ionization of the $3p_j$ levels via a manifold of highly excited Rydberg states of appropriate symmetry. These two pathways contribute to double ionization signal at different intensities following the evolution with wavelength and intensity of the maximum population on the excited ionic state. On the other hand, it is predicted that ionization of ground state Mg^+ contributes insignificantly to Mg^{2+} production for the intensities employed here.

The above experimental and theoretical findings confirm that the aforementioned near-resonant, one-photon $3p^2\ ^1S_0$-$3p3d\ ^1P_1$ radiative coupling is of central importance in the present study performed under presumed unfavorable conditions for double ionization, as far as pulse duration and intensity are concerned. It is thus demonstrated that when relatively long pulses of moderate peak intensity are employed, the doubly excited states above the first ionization threshold of an alkaline-earth-metal atom play a role in the dynamics of double ionization far more crucial than the one currently attributed to them in the context of short-pulse high-intensity experiments. It would be interesting to test the above conclusion to doubly excited ladder systems in other alkaline-earth-metal atoms, such as Ca. Concerning the theory it seems worth attempting a more elaborate description of these complex processes through a unified treatment in the framework of the time-dependent Schrödinger equation (TDSE), although this is a highly nontrivial task when a very large number of photons are involved despite the fact that the intensity is rather moderate. Moreover, the TDSE is not always sufficiently transparent when it comes to identifying the contribution of doubly excited atomic and excited ionic states to the dynamics of double ionization and efficient methods to meet this goal will have to be devised.

ACKNOWLEDGMENTS

The experiment was performed at the Central Laser Facility of the University of Ioannina. One of the authors (A.L.) gratefully acknowledges many enlightening discussions with Dr. H. Bachau as well as the courtesy of Professor B. Piraux who provided us with an original version of the embedded Runge-Kutta routine. This research was funded by the program HERAKLITOS of the Operational Program for Education and Initial Vocational Training of the Hellenic Ministry of Education, under the 3rd Community Support Framework and the European Social Fund.

[1] I. S. Aleksakhin, I. P. Zapesochnyi, and V. V. Suran, JETP Lett. **26**, 11 (1977); I. S. Alexksakhin, N. B. Delone, I. P. Zapesochnyi, and V. V. Suran, Sov. Phys. JETP **49**, 447 (1979).
[2] *Atoms in Intense Laser Fields*, edited by M. Gavrila, Advances in Atomic, Molecular and Optical Physics, Suppl. 1 (Academic, New York, 1992).
[3] P. Lambropoulos, P. Maragakis, and J. Zhang, Phys. Rep. **305**, 205 (1998), and references therein.
[4] H. K. Haugen and H. Stapelfeldt, Phys. Rev. A **45**, 1847 (1992).
[5] Z. Jingyuan, Li Qiongru, Y. Jian, Z. Lizeng, and Nie Yuxin, J. Phys. B **19**, L75 (1985).
[6] D. Kim, S. Fournier, M. Saeed, and L. F. DiMauro, Phys. Rev. A **41**, 4966 (1990).
[7] M. Hou, P. Breger, G. Petite, and P. Agostini, J. Phys. B **23**, L583 (1990).
[8] N. J. van Druten, R. Trainham, and H. G. Muller, Phys. Rev. A **50**, 1593 (1994).
[9] I. I. Bondar and V. V. Suran, JETP Lett. **56**, 78 (1992); JETP **76**, 381 (1993); I. I. Bondar, V. V. Suran, and M. I. Dudich, J. Phys. B **33**, 4243 (2000); I. I. Bondar and V. V. Suran, *ibid.* **35**, 3391 (2002).
[10] D. Xenakis, N. E. Karapanagioti, D. Charalambidis, H. Bachau, and E. Cormier, Phys. Rev. A **60**, 3916 (1999).
[11] G. D. Gillen, M. A. Walker, and L. D. Van Woerkom, Phys. Rev. A **64**, 043413 (2001).
[12] P. Lambropoulos and P. Zoller, Phys. Rev. A **24**, 379 (1981).
[13] N. E. Karapanagioti, D. Charalambidis, C. J. G. J. Uiterwaal, C. Fotakis, H. Bachau, I. Sanchez, and E. Cormier, Phys. Rev. A **53**, 2587 (1996).
[14] W. Ansbacher, Y. Li, and E. H. Pinnington, Phys. Lett. A **139**, 165 (1989).
[15] B. Dai and P. Lambropoulos, Phys. Rev. A **34**, 3954 (1986).
[16] G. Lagmago Kamta, T. Grosges, B. Piraux, R. Hasbani, E. Cormier, and H. Bachau, J. Phys. B **34**, 857 (2001); E. Hairer, S. P. Nørsett, and G. Wanner, *Solving Ordinary Differential Equations I: Nonstiff Problems* (Springer, Berlin, 1987).
[17] A. Lyras and H. Bachau, Phys. Rev. A **60**, 4781 (1999).
[18] X. Tang, A. Lyras, and P. Lambropoulos, Phys. Rev. Lett. **63**, 972 (1989); J. Opt. Soc. Am. B **7**, 456 (1990); H. Rudolph, X. Tang, H. Bachau, and P. Lambropoulos, Phys. Rev. Lett. **66**, 3241 (1991).
[19] The energy levels table of MgII at the web site: http://physics.nist.gov/cgi-bin/AtData/main_asd
[20] M. Edwards, X. Tang, P. Lambropoulos, and R. Shakeshaft, Phys. Rev. A **33**, 4444 (1986); M. Edwards, X. Tang, and R. Shakeshaft, *ibid.* **35**, 3758 (1987).
[21] H. van Regemorter, H. B. Dy, and M. Prud'homme, J. Phys. B **12**, 1053 (1979); H. B. Dy and H. van Regemorter, *ibid.* **12**, L715 (1979).
[22] P. Lambropoulos and X. Tang, J. Opt. Soc. Am. B **4**, 821 (1987).
[23] R. E. Bonanno, C. W. Clark, and T. B. Lucatorto, Phys. Rev. A **34**, 2082 (1986); Y. L. Shao, C. Fotakis, and D. Charalambidis, *ibid.* **48**, 3636 (1993), and references therein.
[24] I. I. Bondar and V. V. Suran, Opt. Spectrosc. **68**, 265 (1990).
[25] M. V. Ammosov, N. B. Delone, M. Yu. Ivanov, I. I. Bondar, and A. V. Masalov, Adv. At., Mol., Opt. Phys. **29**, 33 (1991).
[26] G. N. Gibson, R. R. Freeman, T. J. McIlrath, and H. G. Muller, Phys. Rev. A **49**, 3870 (1994).
[27] P. Bowe, F. Giammanco, R. W. O'Neill, P. J. M. van der Burgt, and J. A. Slevin, Phys. Rev. A **58**, 1389 (1998).
[28] N. J. Kylstra, H. W. Van der Hart, P. G. Burke, and C. J. Joachain, J. Phys. B **31**, 3089 (1998).